Simulation of exciton condensate-mediated quantum transport in a double-monolayer transition metal dichalcogenide system

Xian Wu, Xuehao Mou, Leonard F. Register, and Sanjay K. Banerjee
Microelectronics Research Center, Department of Electrical and Computer Engineering, The University of Texas at Austin, Austin, Texas 78758, USA

(Received 10 April 2018; revised manuscript received 8 December 2018; published 7 January 2019)

We have developed and employed a quantum transport simulation method to study the transport properties in the presence of a spatially indirect exciton condensate between energy-gapped two-dimensional semiconductors, with contact to each end of each layer. This system differs from previous works on bilayer exciton transport properties in the consideration of the energy gap as well as the associated massive (parabolic band structure) electrons and holes. We observe transport properties in the presence of the condensate including the elimination of current counterflow—otherwise phenomenologically analogous to near-perfect Coulomb drag—absent overlap of the conduction and valence bands of opposite layers, as well as substantially greater critical interlayer current for a given assumed bare interlayer coupling.

DOI: 10.1103/PhysRevB.99.035113

I. INTRODUCTION

The condensation of spatially indirect excitons (bound electron-hole pairs) [1] between partially filled Landau levels in opposite layers in III-V double-quantum-well systems [2,3] and, more recently, in a bilayer graphene system [4] under high magnetic fields and low temperatures has been shown experimentally to give rise to novel and interesting transport properties, such as near-perfect interlayer current counterflow (a Coulomb-drag-like current) and ultra-low-voltage interlayer negative differential resistance (NDR). It has been predicted that the interaction between conduction-band (CB) electrons and valence-band (VB) holes in two-dimensional (2D) semiconductor systems such as graphene with a potential for closer proximity of the two layers and in a lower dielectric-constant environment, might allow for such condensates absent the need for the large magnetic fields required to produce the Landau levels, and perhaps at more elevated temperatures [5,6], although only recently has experimental evidence suggesting such excitonic states been found in a bilayer graphene channel-transition metal dichalcogenide (TMD) barrier-bilayer graphene channel system [7], and at still very low temperatures. Beyond the science, it also has been shown that such transport properties could have engineering applications for novel ultra-low-power logic and memory applications [8–10]. More recently, following material advances, use of 2D monolayer TMDs with their massive electrons and holes as the channel material has been predicted to be a better host for such indirect exciton condensates [11–13]. However, the effects of the band gap, as well as of the generally slower carriers, on the transport properties of such systems have not been explored well. These transport properties could have implications both for design of experiments toward observation of exciton condensates in such energy-gapped systems, and for any engineering applications.

In this work, we seek to extend the study of the transport physics and properties in the presence of an exciton condensate from the graphene-based system to gapped 2D semiconductor-based systems via multiband quantum transport simulations. Among our findings is that when the energy bands of the two channel layers no longer overlap, even in the continuing presence of an exciton condensate, not only is the enhanced elastic interlayer tunneling eliminated, but the Coulomb-drag-like current between layers is eliminated.

The remainder of this paper is organized as follows. In Sec. II, we overview our method for simulating the quantum transport in the presence of an exciton condensate in such systems. This method is a combination and extension of the methods we developed in our previous works in Refs. [14–16]. Note that this simulation method is not intended to predict accurately the conditions under which such an exciton condensate can exist, a substantially more challenging and still imperfect science [11–13], but only to predict the basic transport properties in the presence of such a condensate. The 300 K temperature used for all transport simulations in this work is an optimistic by-product of considering only the exchange interaction that drives the condensate formation and associated transport physics of interest here, and not the additional physics that limits actual temperature of condensate formation. In Sec. III, we use this method to study a specific model which captures the key features of interest of the near-band-edge states of TMD monolayers and demonstrate the transport properties in these systems. In Sec. IV, we present a brief summary and conclusions from our study.

II. SIMULATION SYSTEM AND METHOD

The basic system of interest is shown schematically in Fig. 1(a). Two 2D semiconductor monolayers are separated by a tunnel barrier of thickness d within an effective dielectric environment of dielectric constant κ. The electrostatic potentials in these two monolayers are controlled by two external gates, V_{TG} and V_{BG}, which (along with perhaps work

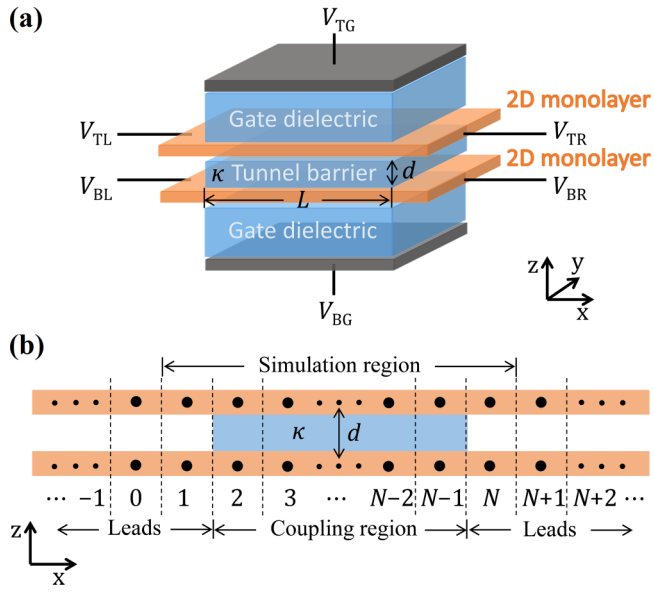

FIG. 1. (a) Schematic structure of the simulation system in this study. (b) Numbering of the atomic unit cells along the transport direction. Interlayer coupling only exists in the region between the $n = 2$ and $n = N - 1$ cells. The wave functions are solved for only unit cells 1 through N; other atomic cells are represented by the absorbing and injecting boundary conditions.

function engineering in any practice) would provide control over the energy band alignments and carrier concentrations of the top and bottom 2D monolayers. In this work, for specificity, the top and bottom layers are always gated to be n-type (electron-type) and p-type (hole-type), respectively, with roughly equal electron and hole concentrations. Top and bottom transport channels (for transport along the $\hat{\mathbf{x}}$ direction in Fig. 1) of length L are formed in the two monolayers between independent semi-infinite leads, top-left (TL) and top-right (TR), and bottom-left (BL) and bottom-right (BR), respectively. These electrical leads are connected to different voltage sources, V_{TL} and V_{TR}, and V_{BL} and V_{BR}, respectively.

In prior works, members of our research group and colleagues introduced simulation tools for simulating quantum transport in graphene-channel based systems in the presence of an exciton condensate [14]. We also have performed quantum transport simulations for a structurally similar TMD-based system, absent a condensate [16], and modeled equilibrium condensate properties in bilayer TMDs [15]. For this work, we have combined elements of these prior studies to allow modeling of transport in the presence of a condensate in a model TMD system, as described in the remainder of this section.

The wave function of a single-electron state in the system, $|\psi\rangle$, is projected into a set of tight-binding basis orbitals, $|n\alpha\rangle$, where the index n labels the bilayer unit cells, and the index α labels the orbitals. Assuming there are M basis orbitals in each bilayer unit cell, the projection coefficients within unit cell n—the tight-binding wave function—can be written as an M by 1 column vector which comprises both top (T) and bottom (B) components depending on the layer in which the basis orbital is centered,

$$\mathbf{\Psi}_n = \begin{bmatrix} \mathbf{\Psi}_{n\mathrm{T}} \\ \mathbf{\Psi}_{n\mathrm{B}} \end{bmatrix}. \tag{1}$$

The M by M Hamiltonian matrices, $\mathbf{H}_{nn'}$, have the form (as in Refs. [15,16])

$$\mathbf{H}_{nn'} = \begin{bmatrix} \mathbf{H}^{(\mathrm{bare})}_{n\mathrm{T};n'\mathrm{T}} + \mathbf{H}^{(\mathrm{ES})}_{n\mathrm{T};n'\mathrm{T}} & \mathbf{H}^{(\mathrm{bare})}_{n\mathrm{T};n'\mathrm{B}} + \mathbf{H}^{(\mathrm{Fock})}_{n\mathrm{T};n'\mathrm{B}} \\ \mathbf{H}^{(\mathrm{bare})}_{n\mathrm{B};n'\mathrm{T}} + \mathbf{H}^{(\mathrm{Fock})}_{n\mathrm{B};n'\mathrm{T}} & \mathbf{H}^{(\mathrm{bare})}_{n\mathrm{B};n'\mathrm{B}} + \mathbf{H}^{(\mathrm{ES})}_{n\mathrm{B};n'\mathrm{B}} \end{bmatrix}, \tag{2}$$

where the superscripts "bare," "ES," and "Fock" denote the bare tight-binding transfer integrals, the electrostatic potential energies, and the Fock exchange interactions, respectively. These components are set as follows: the bare tight-binding transfer matrix, $\mathbf{H}^{(\mathrm{bare})}$, can be, depending on the basis orbitals being used, the empirical hopping energies between atomic orbitals, or the extracted hopping parameters between maximally localized Wannier functions [17] based on density functional theory (DFT) calculations; the top (bottom) intralayer electrostatic term, $\mathbf{H}^{(\mathrm{ES})}$, is simply set by

$$\mathbf{H}^{(\mathrm{ES})}_{n\mathrm{T(B)};n'\mathrm{T(B)}} = -q\varphi_{n\mathrm{T(B)}}\delta_{nn'}\mathbf{I}, \tag{3}$$

where q is the unit charge, $\varphi_{n\mathrm{T(B)}}$ is the average electrostatic potential of the top (bottom) layer within unit cell n, $\delta_{nn'}$ is the Kronecker delta function, and $\mathbf{I}$ is the unit matrix; and the interlayer Fock exchange interaction, $\mathbf{H}^{(\mathrm{Fock})}$, is calculated by the elementwise multiplication (Hadamard product, indicated by "$\circ$") of the Coulomb matrix $\mathbf{V}$ and the density matrix $\boldsymbol{\rho}$, i.e.,

$$\mathbf{H}^{(\mathrm{Fock})}_{n\mathrm{T};n'\mathrm{B}} = \mathbf{H}^{(\mathrm{Fock})\dagger}_{n'\mathrm{B};n\mathrm{T}} = -\mathbf{V}_{n\mathrm{T};n'\mathrm{B}} \circ \boldsymbol{\rho}_{n\mathrm{T};n'\mathrm{B}}. \tag{4}$$

Here, each element of $\mathbf{V}_{n\mathrm{T};n'\mathrm{B}}$ represents the Coulomb interaction between an electron centered at $\mathbf{r}_{n\mathrm{T}\alpha}$ in the top layer and another electron centered at $\mathbf{r}_{n'\mathrm{B}\alpha'}$ in the bottom layer, i.e.,

$$[\mathbf{V}_{n\mathrm{T};n'\mathrm{B}}]_{\alpha\alpha'} = q^2/(4\pi\kappa\varepsilon_0|\mathbf{r}_{n\mathrm{T}\alpha} - \mathbf{r}_{n'\mathrm{B}\alpha'}|), \tag{5}$$

where ε_0 is the vacuum permittivity, and the density matrix $\boldsymbol{\rho}_{n\mathrm{T};n'\mathrm{B}}$ is calculated as

$$\boldsymbol{\rho}_{n\mathrm{T};n'\mathrm{B}} = \sum_{\beta} f(\beta)\mathbf{\Psi}_{n\mathrm{T}}(\beta)\mathbf{\Psi}^{\dagger}_{n'\mathrm{B}}(\beta), \tag{6}$$

where β labels an electron state, and $f(\beta)$ is the occupation probability of the state, which, in this work, is described by the Fermi-Dirac distribution of the lead of injection with Fermi levels (chemical potentials) $E_{\mathrm{F},l}$ determined by the supply voltages as $E_{\mathrm{F},l} = -qV_l$ for each l = TL, TR, BL, and BR. In this way, the change in any individual tight-binding wave function, $\Psi_{n'}(\beta')$, or its occupation probability, $f(\beta')$, affects all wave functions, $\Psi_n(\beta)$, self-consistently.

We assume that the system is wide and translationally invariant in the direction normal to the transport direction, such that a wave vector k_y can be used to calculate the variation of $\mathbf{\Psi}_n$ among unit cells along this transverse direction $\hat{\mathbf{y}}$ for each unit cell slice along the transport direction $\hat{\mathbf{x}}$, using the Bloch's theorem. We label the unit cells in one slice along the transport direction as shown in Fig. 1(b), where the $n = 1$ and $n = N$ cells are the boundary cells of the simulation region, and apply the similar method as in Ref. [16] to set up a transport equation in the channel to solve for the electron states described by an

$N \cdot M$ by 1 vector $\mathbf{\Psi}$ with N components $\mathbf{\Psi}_n (n = 1, \ldots, N)$ defined by Eq. (1) for each considered energy E and wave vector k_y,

$$(E\mathbf{I} - \mathbf{H} - \mathbf{\Sigma})\mathbf{\Psi} = \mathbf{S}, \tag{7}$$

where again, N is the number of unit cells along the transport direction in the simulation region, and M is the number of orbitals in each unit cell; $\mathbf{H}$ is the $N \cdot M$ by $N \cdot M$ Hamiltonian matrix, with $\mathbf{H}_{nn'}(n, n' = 1, \ldots, N)$ defined by Eq. (2) as its blocks; and the source vector $\mathbf{S}$ and self-energy matrix $\mathbf{\Sigma}$ describe the boundary conditions. The source and self-energy components, $\mathbf{S}_n$ and $\mathbf{\Sigma}_{nn'}$, are all zeros except for $\mathbf{\Sigma}_{11} = \mathbf{H}_{10}\mathbf{T}_-$, $\mathbf{S}_1 = \mathbf{H}_{10}(\mathbf{I} - \mathbf{T}_-\mathbf{T}_+)\mathbf{\Psi}_0^+$, $\mathbf{\Sigma}_{NN} = \mathbf{H}_{N(N+1)}\mathbf{T}_+$, and $\mathbf{S}_N = \mathbf{H}_{N(N+1)}(\mathbf{I} - \mathbf{T}_+\mathbf{T}_-)\mathbf{\Psi}_{N+1}^-$. Here, $\mathbf{\Psi}_0^+$ ($\mathbf{\Psi}_{N+1}^-$) is the extension into the boundary of the simulation region at $n = 0$ ($n = N + 1$) of an incident eigenstate of the left (right) top or bottom lead. (Wave functions resulting from injection from top or bottom leads, as well as left and right leads, are calculated separately.) $\mathbf{T}_+$ ($\mathbf{T}_-$) is used to calculate the response of the $n = 1$ ($n = N$) boundary cell with this injection by $\mathbf{\Psi}_1^+ = \mathbf{T}_+\mathbf{\Psi}_0^+$ ($\mathbf{\Psi}_N^- = \mathbf{T}_-\mathbf{\Psi}_{N+1}^-$). $\mathbf{\Psi}_0^+$, $\mathbf{\Psi}_{N+1}^-$, and $\mathbf{T}_\pm$ are similarly constructed using the solutions of the quadratic eigenvalue equation for the lead Bloch functions with the same energy E in Eq. (7), characterized by the unit-cell-to-unit-cell phase shift λ and the intra-unit-cell tight-binding wave function represented by the M by 1 vector $\mathbf{\Phi}$,

$$(\mathbf{H}_{10} + \lambda\mathbf{H}_{00} + \lambda^2\mathbf{H}_{01})\mathbf{\Phi} = \lambda E\mathbf{\Phi}, \tag{8}$$

as in Ref. [16]. Equation (7) is solved for every state β spanning over energy E, wave vector k_y, injection lead l, and injection band i. The solutions are then fed back to update the density matrix $\boldsymbol{\rho}$ in Eq. (6), which leads to a new set of solutions to Eq. (7). These two steps are iterated until convergence is achieved. The steady-state current that flows between any two unit cells in the system then is calculated from

$$I_{n\to n'} = \frac{-2q}{\hbar}\sum_\beta f(\beta)\,\mathrm{Im}[\mathbf{\Psi}_{n'}^\dagger(\beta)\mathbf{H}_{n'n}\mathbf{\Psi}_n(\beta)]. \tag{9}$$

The approach described by Eqs. (1)–(9) above can be used to simulate similar bilayer systems using arbitrary basis functions and hopping potentials. However, to study the essential quantum transport physics, in this paper we consider only a simplified multiband model as follows. For both layers, we use the 2D lattice structure of a MoS_2 monolayer with lattice constant $a = 3.16$ Å and assume two orbitals centered at the Mo atoms in each primitive unit cell. To limit unit cell sizes as matter of practicality, we assume rotational alignment between the top and bottom MoS_2 layers, such as has been achieved in analogous graphene systems [18,19]. However, we note that condensate formation is not dependent on rotational alignment [20], and that rotational misalignment could indeed be useful to limit the bare interlayer coupling while still maximizing the proximity of the 2D semiconductors to maximize the electrostatic and, thus, exchange interaction. We consider only the hopping parameters between the nearest unit cells and the on-site potentials in the same unit cells for the intralayer bare hopping matrices, $\mathbf{H}^{(\mathrm{bare})}_{n\mathrm{T};n'\mathrm{T}}$ and $\mathbf{H}^{(\mathrm{bare})}_{n\mathrm{B};n'\mathrm{B}}$, in Eq. (2) [see Fig. 2(a)]. These hopping parameters are

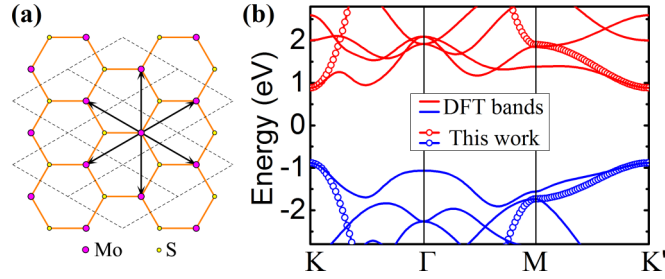

FIG. 2. (a) 2D lattice structure of a MoS_2 monolayer used in this study. Dashed lines show the unit cells. We only consider the hopping parameters between the Mo atom-centered orbitals up to the nearest unit cells. (b) Comparison between the band structure calculated using the hopping parameters in this work and those extracted from the density functional theory (DFT) calculations.

adjusted to match the CB and VB edge effective masses of a MoS_2 monolayer. We use a CB edge (electron) effective mass of $m_e^* = 0.5m_0$ and a VB edge (minus hole) effective mass of $-m_h^* = -0.6m_0$ to fit these parameters, where m_0 is the free-space electron rest mass. This method is able to capture the band-edge states of the MoS_2 monolayer as shown by the band structure comparison between this model and that from DFT calculations in Fig. 2(b). Note that this model does not address the significant VB spin-splitting observed in TMDs. Albeit more accurate models are available (e.g., the model in Ref. [15]), this simplified model is sufficient for the qualitative study of the essential physics of the quantum transport phenomena in this system with fewer computational resources and faster convergence. Moreover, the interlayer bare-hopping matrices, $\mathbf{H}^{(\mathrm{bare})}_{n\mathrm{T};n'\mathrm{B}}$, are critical to determine, e.g., the critical interlayer current [14,21], analogous to the critical current of a Josephson junction. For the qualitative purposes of this work, we take the effective interlayer bare-hopping to be of the simple form,

$$\mathbf{H}^{(\mathrm{bare})}_{n\mathrm{T};n'\mathrm{B}} = \mathbf{H}^{(\mathrm{bare})}_{n'\mathrm{B};n\mathrm{T}} = t\mathbf{I}\delta_{nn'}, \tag{10}$$

where the coupling constant t between like top and bottom layer orbitals within the same unit cell only represents bare interlayer coupling which would vary with interlayer dielectric material, dielectric thickness, and even rotational alignment of the dielectric with the MoS_2 layers [22].

III. SIMULATION RESULTS

To focus on the essential transport properties in the system, in this work we study the current flows in response to various voltages. For specificity, we use fixed parameters including a channel length of $L = 10$ nm, an effective position-independent dielectric constant of $\kappa = 2.2$, a tunnel barrier thickness of $d = 1$ nm, and a temperature $T = 300$ K throughout this paper, which remains sufficient for establishing an exciton condensate within the simplified model of this work. We consider three limiting biasing conditions. In Sec. III A, we consider the equilibrium condition under which the four leads are all grounded, i.e., $V_{\mathrm{TL}} = V_{\mathrm{BL}} = V_{\mathrm{TR}} = V_{\mathrm{BR}} = 0$; in Sec. III B, we address the "current counterflow" (phenomenologically, Coulomb-drag-like) intralayer biasing condition under which the bottom leads are biased

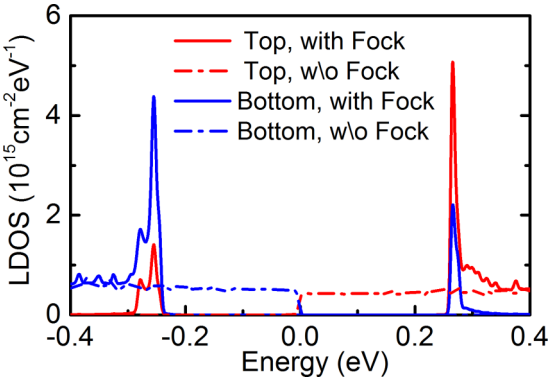

FIG. 3. Local density of states (LDOS) at the center of the channel when the system is in equilibrium, with and without the Fock exchange interaction. The tCB and bVB in the leads are just touching, corresponding to a carrier concentration of $n = p \approx 7 \times 10^{12}$ cm^{-2}. The interlayer bare coupling energy is $t = 0.5$ meV. There is a 500 meV energy gap when the Fock exchange interaction is present.

with a voltage difference V_b, and the top leads are grounded, such that $V_{BL} = -V_{BR} = V_b/2$ and $V_{TL} = V_{TR} = 0$; and in Sec. III C, we discuss an "interlayer" biasing condition under which the two left leads are biased with an interlayer voltage difference V_l, and the right leads are grounded, such that $V_{TL} = -V_{BL} = V_l/2$ and $V_{TR} = V_{BR} = 0$. In addition to these lead biasing conditions, there are two distinct gating scenarios of how the top (electron) layer CB (tCB) and the bottom (hole) layer VB (bVB) edges are aligned in the leads, and would be aligned throughout the simulation region in the absence of the condensate: in one there is an energy gap between the tCB and bVB, and the other the tCB and bVB overlap in energy. In Sec. III A through Sec. III C, for conceptual clarity, we vary the electrostatic potentials in the channel—and, thus, the band edges in the absence of condensate formation—independent of the applied lead voltages (which in practice would require substantial counteradjustments to gate voltages for each variation of lead voltage). In Sec. III D, we will consider self-consistent variations in the electrostatic potential in the channel with lead voltages due to nonzero (and substantial) channel quantum capacitances [23].

A. Equilibrium

In our previous study looking at the equilibrium bulk (translational invariance of the potential among unit cells in both in-plane directions of the 2D monolayers) exciton condensate properties [15], we observed a condensate-induced energy gap of hundreds of meV, which was roughly independent of the nominal alignment of the energy bands of the top and bottom layers absent the condensate, and which corresponded to the exciton binding energy, as long as the nominal (condensate free) band edges are not separated by more than this binding energy. In the system of this study, with the condensate localized between the leads, condensate formation is recognized in the local density of states (LDOS) away from the open simulation region boundaries, as shown in the center of the simulation region in Fig. 3. The induced interlayer energy gap in the LDOS remains roughly unchanged no matter how the nominal tCB and bVB are initially aligned, as long as they are not separated by more than this condensate induced gap.

B. Intralayer biasing

With our simulation parameters, when the gates are biased such that there is an energy gap between the tCB and bVB in the leads, this gap prohibits elastic carrier transfer from one layer to the other independent of condensate formation. For example, with the ideal gate control of the band alignments currently considered, when the carrier concentrations are gated to 5×10^{12} cm^{-2} in both layers, there is a 30 meV gap between the tCB and bVB in the leads. Moreover, current flow between the leads along the layers in the channel is blocked by the condensate-induced energy gap in the LDOS, beyond a small current associated with the tails of the thermal distribution, at least when the condensate-induced gap in the LDOS in the channel is larger than the condensate-free gap between the tCB and bVB, as illustrated schematically and shown via simulations in Fig. 4. Thus a reduction, if not elimination, of intralayer current flow becomes one candidate experimental signature of condensate formation in such gapped bilayer systems, even if perhaps at much lower temperatures and smaller energy gaps.

When the gate voltages cause the tCB and bVB to overlap, however, with bias voltages applied to the bottom leads we observe equal magnitude steady-state currents flowing into the BL lead and out the BR lead with the same 10 mV bias voltage applied, despite the continuing existence of the condensate-induced band gap in the LDOS in the channel. Moreover, in the top layer, currents of almost same magnitude flow, but in the opposite channel direction, into the TR lead and out TL lead, although these two leads are grounded, as seen in Fig. 5(a). However, at the energies of the injected/extracted carriers to/from the leads, this current counterflow is actually composed of interlayer currents flowing in opposite directions between the lead pairs at the opposite ends of the channels, BL to TL lead and TR to BR lead, respectively, but much larger than would be produced by the bare-coupling-induced tunneling alone. These interlayer currents are mediated by coupling via the self-consistent nonlocal Fock exchange interaction within the many-body exciton condensate to a mutually excited counterclockwise current loop along and between the layers below the condensate-induced energy gap, as illustrated in Fig. 6(c) with current subdivided above and below a cutoff energy E_{co} chosen well below the Fermi levels, but above the bottom of this gap. Thus the condensate leads to a near perfect Coulomb-drag-like behavior at the leads within, but only within where the nominal tCB and bVB overlap, as shown in Fig. 7. This near-perfect Coulomb-drag-like behavior is another signature of exciton condensate formation, as already observed in experimental III-V systems [2,3] and illustrated in our prior simulation of graphene systems [14], but in, and only in, this region of interlayer band overlap with these gapped semiconductors.

C. Interlayer biasing

As noted in Sec. III B above and shown in Fig. 4, condensate or not, no current can flow between the layers even

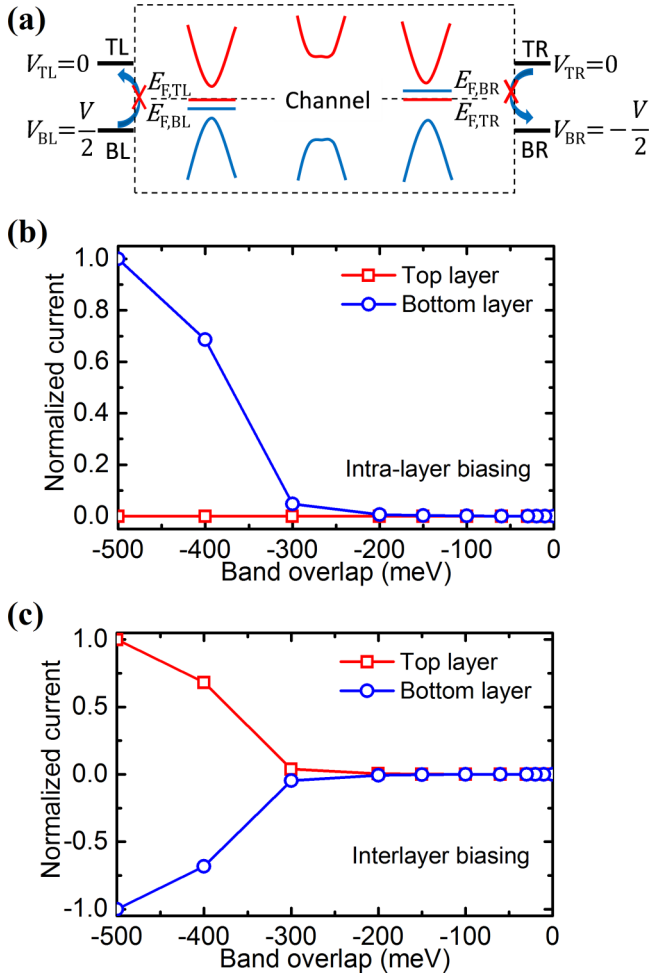

FIG. 4. (a) Illustration of the band alignment when the tCB and bVB do not overlap, which prevents intralayer and interlayer current flow under intralayer (or interlayer) biasing. (b) Intralayer currents in top and bottom layers normalized to the corresponding values without the Fock exchange interaction, as functions of the overlap between tCB and bVB under intralayer biasing with $V_b = 10$ mV. The interlayer bare coupling energy is $t = 0.5$ meV, the positive direction of the current is from left to right, and a negative overlap means the two bands do not overlap. (c) Same curves as in (b), except that the system is under interlayer biasing with $V_l = 10$ mV. In both (b) and (c), as tCB and bVB are brought close to each other, exciton condensate formation begins to expand band gap in the channel and, thus, blocks the intralayer current as long as tCB and bVB do not overlap. No intralayer current can exist in this nonoverlapped-bands scenario.

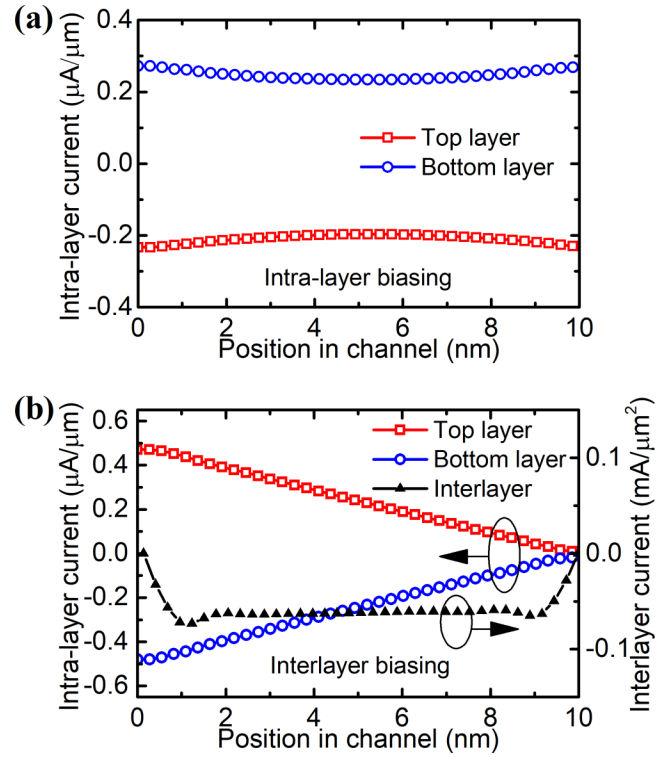

FIG. 5. Current distribution along the channel under (a) intralayer biasing with bias voltage $V_b = 10$ mV, and (b) interlayer biasing with bias voltage $V_l = 10$ mV. The positive sign for the intra- and interlayer current means the direction from left to right and from bottom to top, respectively. However, under the intralayer biasing, the total interlayer current is negligible thus it's not shown. The tCB and bVB have an overlap of 15 meV. The interlayer bare coupling energy is $t = 0.5$ meV.

with interlayer bias voltage applied when the tCB and bVB do not overlap. When there is such overlap in the presence of an exciton condensate, however, we observe an enhanced interlayer tunneling current as compared to the case without the exciton condensate if we apply a small interlayer voltage to the end leads as shown in Fig. 5(b). By analyzing the current components from electrons with energy below and above the cutoff energy E_{co} in Fig. 6(d) as done for intralayer biasing, we find here, as for the graphene system before [14], that the enhanced current flow near the Fermi level is restricted to near the left leads and is associated with a counterflowing current near the left leads that flows below the condensate-induced gap (below E_{co}), which, in turn, is then balanced by more current flow below E_{co} along and in the opposite direction between the layers. Negligible current flows out of the right leads, so that they could be floating; they are not necessary to this process. These behaviors are schematically explained by Fig. 6(b).

However, also as in the simulated graphene system [14] and the experimental III-V systems [21], the amount of interlayer current that can flow in this way is limited. In principle, this current can be reached at very low voltages depending on the interlayer bare coupling, leading to a very low voltage NDR, even at voltages below $k_B T$ (where k_B is the Boltzmann constant) in principle, which could have novel applications in memory and unconventional logic [8–10]. As derived in Ref. [14], the interlayer current mediated by the condensate between a pair of orbitals, one of which resides in the top layer and the other resides in the bottom layer, is

$$I = \frac{-2q}{\hbar} t|\rho| \sin[\arg(\rho)], \tag{11}$$

where t is the interlayer bare coupling energy and ρ is the density matrix element between the two orbitals. With the tCB and bVB overlap fixed, the absolute value of ρ is largely independent on the small bias voltages. However, the

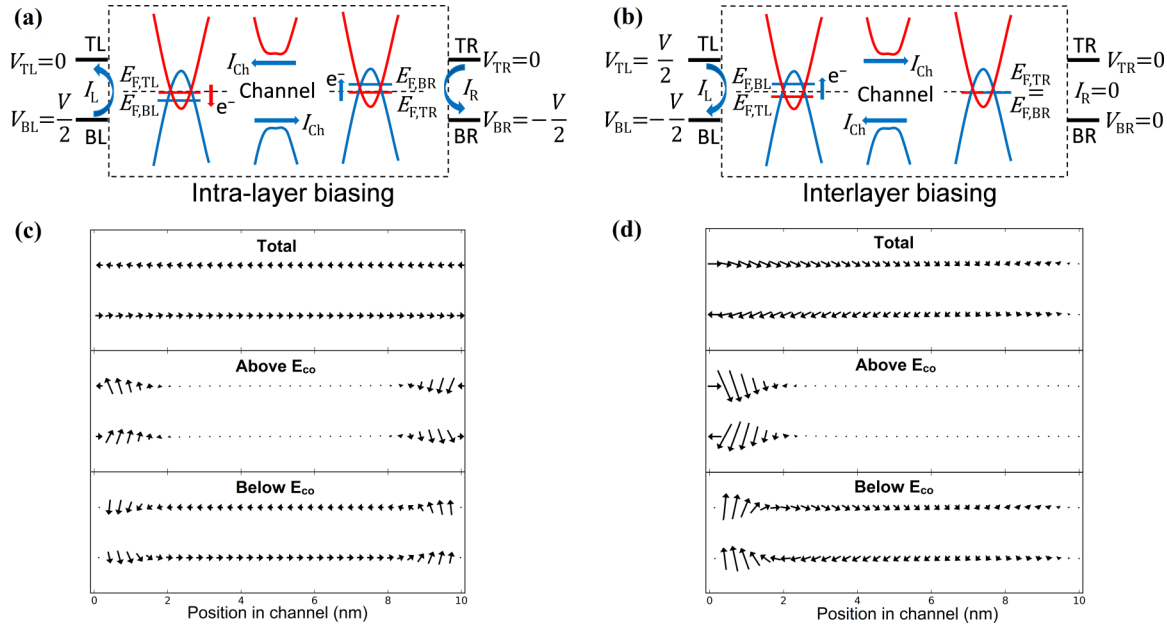

FIG. 6. Illustration of the band alignment and current flow under (a) intralayer biasing, and (b) interlayer biasing, both when the tCB and bVB overlap with each other, and visualization of the total current, as well as its components across the top and bottom layers for (c) intralayer biasing, and (d) interlayer biasing, from carriers with energy below and above a cutoff energy $E_{co} \approx -100$ meV relative to the zero bias Fermi level (but above the bottom of the condensate-induced band gap), obtained with the same parameters as used in Fig. 5. The horizontal component of each arrow represents the magnitude and direction of the intralayer current, and the vertical component represents the interlayer current. However, the scales of the magnitude of the two components are not directly comparable since intra- and interlayer currents have different units.

argument (phase) of ρ, which is the collective "pseudospin phase" of all interlayer pairs of orbitals, shifts toward the direction that increases $|\sin[\arg(\rho)]|$ as the bias voltages increase. If a voltage larger than that induces a critical current of $I_C = 2qt|\rho|/\hbar$ is applied, the steady-state current collapses

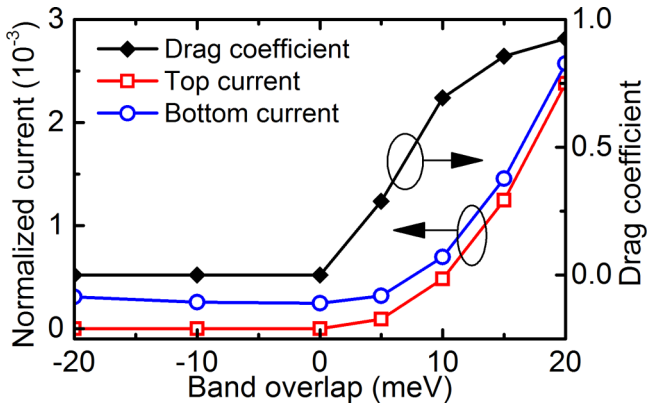

FIG. 7. The intralayer current, under intralayer biasing, of both layers measured at the left leads, normalized to the value without the Fock exchange interaction, and the apparent "Coulomb-drag" coefficient which is defined as the ratio of the current (seemingly) flowing in the passive (top) layer to that in the active (bottom) layer, both as functions of the overlap between tCB and bVB. A negative overlap means the two bands do not overlap. A Coulomb-drag-like current can be seen only when the two bands overlap. The intralayer bias voltage in the bottom layer is fixed at $V_b = 10$ mV. The interlayer bare coupling energy is $t = 0.5$ meV.

because $|\sin[\arg(\rho)]|$ cannot exceed unity and Eq. (11) cannot be satisfied. In our steady-state simulations, we cannot follow the interlayer current with the applied voltage beyond the point at which I_C is reached, and it becomes increasing difficult to converge the iterative calculations as I_C is approached. However, by analyzing the pseudospin phase $\arg(\rho)$ between any interlayer pair of orbitals in the channel along with the current value I flowing from TL to BL, the maximum current from TL to BL which drives the system into the critical condition can be estimated as $I_C = I/\sin[\arg(\rho)]$. I_C calculated in this way as a function of the interlayer bare coupling energy is shown in Fig. 8(a).

The interlayer I-V characteristics of such TMD material-based system also can behave qualitatively differently from those of the graphene-based systems, as shown in Fig. 8(b). Because of the finite overlap of the tCB and bVB, if the Fermi level difference between TL and BL leads exceeds the band overlap before the critical current is reached, the interlayer current saturates rather than collapses. Moreover, by gating this overlap, the system can act much like a conventional tunneling field-effect transistor [24], except with near-unity transmission probability in the presence of a condensate. The dependence of the interlayer current on this overlap is shown in Fig. 9.

Similar to above, this enhanced interlayer current with overlap of the tCB and bVB is yet another signature of exciton condensate formation, as also already observed in experimental III-V systems [21] and illustrated in our prior simulation of the graphene system [14], although with qualitative different dependencies on interlayer voltage possibly.

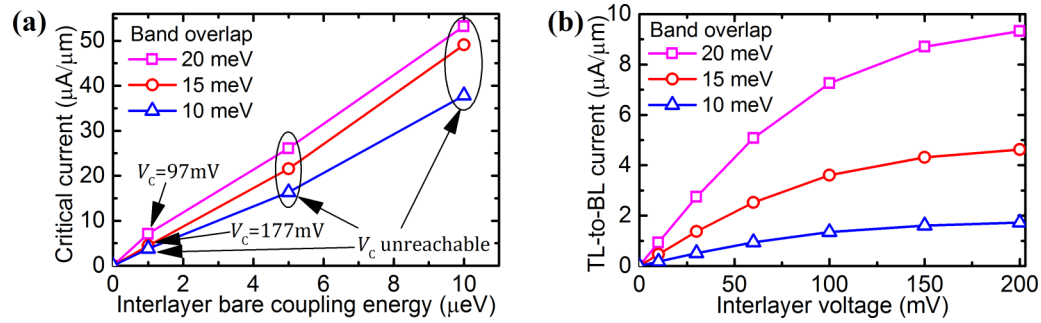

FIG. 8. (a) Estimated critical current I_C that could flow from TL to BL as a function of the interlayer bare coupling energy t under interlayer bias, based on extrapolation from low bias interlayer condensate phase. With a fixed energy overlap between tCB and bVB—here, 10, 15, or 20 meV, I_C has an essentially linear dependence on t. However, the absolute value of the density matrix element, $|\rho|$, increases slightly as the band overlap increases, thus I_C also increases as implied by Eq. (11). (b) The I-V characteristics of the current flowing from TL to BL as a function of the bias voltage V_l with different overlaps between tCB and bVB for a larger interlayer bare coupling $t = 0.5$ meV. (t does not affect the shape of the I-V curves if I_C is not reached.) In the latter figure, the current begins to saturate as the Fermi level separation exceeds the overlap of the tCB and bVB by a few k_BT (∼26 meV at the considered temperature $T = 300$ K). The associated critical voltages V_C, labeled in (a), is estimated from a linear interpolation between two neighboring data points in (b), which produces the same I_C in (a). If I_C is larger than the saturation current, the critical voltage cannot be reached.

D. Lead bias control over the band alignment

So far, the electrostatic potentials in the channel simply have been specified. To simulate the I-V characteristics of the system more realistically, we now consider how these potentials are controlled by the gate as well as bias voltages. Rigorously, these potentials must be solved self-consistently as functions of position in the channel using the Poisson's equation in addition to the iterations of Eqs. (6) and (7) in Sec. II. However, this treatment will add another layer of self-consistent calculations and blur the qualitative focus of this study. Here we assume that the potentials are uniform across the channel, i.e., $\varphi_{n,\mathrm{T}} = \varphi_\mathrm{T}$ and $\varphi_{n,\mathrm{B}} = \varphi_\mathrm{B}$ for every unit cell n, and are determined by the capacitive relations,

$$q(p_\mathrm{T} - n_\mathrm{T}) = C_\mathrm{TG}\Delta\varphi_\mathrm{TG} + C_\mathrm{I}(\varphi_\mathrm{T} - \varphi_\mathrm{B}), \quad (12a)$$

$$q(p_\mathrm{B} - n_\mathrm{B}) = C_\mathrm{BG}\Delta\varphi_\mathrm{BG} + C_\mathrm{I}(\varphi_\mathrm{B} - \varphi_\mathrm{T}), \quad (12b)$$

where C_TG (C_BG) is the top (bottom) gate dielectric capacitance, $C_\mathrm{I} = \kappa\varepsilon_0/d$ is the capacitance of the interlayer dielectric, $\Delta\varphi_\mathrm{TG}$ ($\Delta\varphi_\mathrm{BG}$) is the potential drop across the top (bottom) gate dielectric, and n_T (n_B) and p_T (p_B) are the nominal electron and hole concentrations in the top (bottom) layer without the Fock exchange interaction. Here, we have assumed that the channels are undoped. The electron and hole concentrations of the top channel can be calculated as

$$n_\mathrm{T} = \sum_{l=\mathrm{TL,TR}} \int_{E_{\mathrm{C,T}}(\varphi_\mathrm{T})}^{+\infty} dE\, f_l(E) g_\mathrm{T}(E, \varphi_\mathrm{T})/2, \quad (13a)$$

$$p_\mathrm{T} = \sum_{l=\mathrm{TL,TR}} \int_{-\infty}^{E_{\mathrm{V,T}}(\varphi_\mathrm{T})} dE\, h_l(E) g_\mathrm{T}(E, \varphi_\mathrm{T})/2, \quad (13b)$$

where $f_l(E) = 1/[1 + e^{(E-E_{\mathrm{F},l})/k_\mathrm{B}T}]$ and $h_l(E) = 1 - f_l(E)$, respectively, are the Fermi distribution functions of an electron and a hole state in lead l with Fermi level $E_{\mathrm{F},l}$ controlled by its bias voltage; $E_{\mathrm{C,T}}(\varphi_\mathrm{T})$ and $E_{\mathrm{V,T}}(\varphi_\mathrm{T})$ are the CB and VB edges, respectively, of the top layer under potential φ_T; and $g_\mathrm{T}(E, \varphi_\mathrm{T})$ is the density of states of the top layer under potential φ_T calculated using the band structure of the top layer. The "1/2" factor at the end is because only half of the incident lead states contribute to the carrier concentrations in the channel. By replacing all subscripted top ("T") values with bottom ("B") values and summing over the bottom leads, we similarly are able to calculate the electron and hole concentrations in the bottom layer (n_B and p_B).

The potential drops across the gate dielectrics, $\Delta\varphi_\mathrm{TG}$ and $\Delta\varphi_\mathrm{BG}$, are linked to the gate voltages through various material parameters using the band diagram as in Ref. [24] by

$$q\Delta\varphi_\mathrm{TG} = W_\mathrm{TG} - qV_\mathrm{TG} - \chi_\mathrm{T} - E_{\mathrm{C,T}}(\varphi_\mathrm{T}), \quad (14a)$$

$$q\Delta\varphi_\mathrm{BG} = W_\mathrm{BG} - qV_\mathrm{BG} - \chi_\mathrm{B} - E_{\mathrm{C,B}}(\varphi_\mathrm{B}), \quad (14b)$$

where W_TG (W_BG) is the work function of the top (bottom) gate and χ_T (χ_B) is the effective electron affinity of the top (bottom) channel.

With Eqs. (13) and (14), φ_T and φ_B can be obtained using Eqs. (12) and then used in the iterations of Eqs. (6) and (7) in Sec. II. This method is equivalent to adding four effective

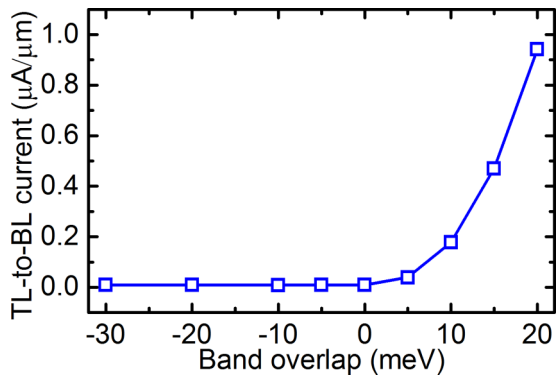

FIG. 9. The current from TL to BL as a function of the overlap between tCB and bVB under a fixed interlayer bias voltage $V_l = 10$ mV. The interlayer bare coupling energy is $t = 0.5$ meV. A negative overlap means the two bands do not overlap. The elastic current necessarily vanishes if the two bands do not overlap.

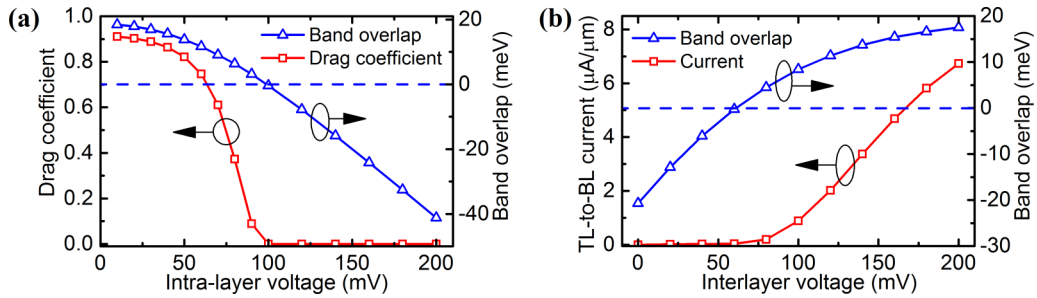

FIG. 10. (a) The dependence of drag coefficient (as defined in Fig. 7) on bias voltage obtained using the electrostatic model in Sec. III D under intralayer biasing with fixed gate voltage $V_{TG} = -V_{BG} = 3.6$ V. (b) TL-to-BL current under interlayer biasing with fixed gate voltage $V_{TG} = -V_{BG} = 3.2$ V using the same model. In both figures, the interlayer bare coupling energy is $t = 0.5$ meV. The corresponding overlap between tCB and bVB also is shown in the same plots (a negative overlap means the two bands do not overlap).

quantum capacitors between each lead and the channel [23]. In this work for specificity, we use work functions $W_{TG} = W_{BG} = 5.1$ eV (e.g., gold) and electron affinities $\chi_T = \chi_B = 4.2$ eV (monolayer MoS_2). The top and bottom gate dielectric capacitances, C_{TG} and C_{BG}, respectively, are taken to be the same as that of the interlayer tunnel barrier, i.e., $C_{TG} = C_{BG} = C_I = 1.9\ \mu F/cm^2$. (As shown above, condensate formation greatly enhances the interlayer coupling. Moreover, independent of the condensate formation, recent work suggests that by rotating the interlayer dielectric, tunneling currents can be varied significantly [22]. Thus it is reasonable to consider using the same barrier material for the gate and tunnel dielectrics.) Using this model and the above parameters, a gate voltage of $V_{TG} = -V_{BG} \approx 3.4$ V brings the tCB edge to just touch the bVB edge when all the four leads are grounded. However, we note that the gate voltages are varied by only ± 200 mV for subsequent simulations, thus this voltage is still more than is required to achieve the potentially useful behaviors observed in these simulations.

With the gate voltages fixed, the bias voltages under the interlayer and the intralayer biasing conditions have different effects on φ_T and φ_B, and consequently the tCB and bVB alignment, which further distinguishes the I-V characteristics for these two biasing conditions. Under the intralayer biasing condition, a positive voltage applied to the BL lead tends to pull the bVB downward with the Fermi level as a result of the quantum capacitance $C_{Q,BL}$ in the channel (which is substantially larger than that in the graphene-based system), while a negative voltage applied to the BR lead tends to pull it upward. However, the former effect is more pronounced because it's toward the direction that $C_{Q,BL}$, itself, increases. Therefore as the intralayer bias voltage increases, the band overlap shrinks, which further reduces or even eliminates the Coulomb-drag-like current [see Fig. 10(a)]. This behavior is symmetric with respect to positive and negative intralayer voltages. Under interlayer biasing, a positive bias voltage applied to the TL lead tends to pull the tCB downward and the negative voltage applied to the BL lead tends to bring the bVB upward. Therefore, the overlap between the two bands increases with an increasing positive interlayer bias, and decreases with an increasingly negative interlayer bias. This interlayer bias control alters the I-V characteristics of Fig. 8(b) in two ways, as shown in Fig. 10(b); it introduces a shift of the threshold voltage associated with aligning the tCB edge and bottom bVB edge, which can be negative or positive depending on the interlayer bias; and it changes the shape of I-V curve by varying the tCB and bVB overlap in addition to the Fermi level difference.

IV. SUMMARY AND CONCLUSIONS

In conclusion and summary, we have studied the current flow in a TMD monolayer-based four-lead bilayer system in the presence of the spatially indirect exciton condensate using a quantum transport simulator. The exciton condensate is induced by the nonlocal interlayer Fock exchange interaction, which is calculated self-consistently along with the multiband quantum transport equation. These simulations are not intended to predict accurately the conditions under which such an exciton condensate can exist, but only to predict the transport properties in the presence of such a condensate. These reported behaviors may aid in the interpretation of experimental efforts to observe exciton condensates in such systems, as well as for potential device applications.

With gapped parabolic band structures of the model TMD monolayers, this system exhibits some of the same properties exhibited in prior experimental and theoretical works, but also properties specific to this gapped system. The parabolic bands and associated massive carriers in the TMD monolayers lead to larger exciton binding energies than the zero-band-edge-mass carriers in the graphene system. This result should be beneficial for forming and maintaining the condensate, and leads to a larger critical current for a given interlayer bare coupling strength before the current becomes time-dependent (or fails to reach a steady-state solution in these time-independent calculations), defining the onset of a potentially strong and very low voltage NDR, as seen in experimental exciton condensates [21] and in a previously simulated graphene-based system [14]. This increase in critical current, however, could be either beneficial or detrimental depending on the achievable interlayer bare coupling and desired mode of operation. Under interlayer biasing, unlike for the graphene based system, the interlayer elastic current, perhaps self-evidently, can be eliminated by removing overlap at the leads between the charged electron band (tCB) and hole band (bVB), even in the presence of the condensate. Perhaps less self-evidently, the near-perfect Coulomb-drag-like counterflow current under intralayer bias also is eliminated by the lack of such

interlayer band overlap. This latter current actually consists of interlayer currents flowing between and near the Fermi levels in opposite directions at opposite ends of the channel, thus subject to the same requirement for band overlap as the interlayer-bias-induced current. Moreover, with band overlap, both the enhanced interlayer current under interlayer bias and the counterflow current under intralayer bias are supported by coupling through the condensate to currents flowing below the condensate-induced gap.

Also, in the TMD-based system, large channel quantum capacitance (associated with the large density of states) makes the electrostatic profiles along the channel sensitive to the terminal bias voltages. Therefore in addition to changing the Fermi level differences, the bias voltages also change the alignment of the tCB and bVB, which has additional effects on the current, including creating nonzero thresholds for either intralayer or interlayer current flow in terms of the bias voltages, which is associated with the onset of overlap of conduction-to-valence band overlap between the TMD layers.

These simulated behaviors offer mechanisms for experimentally identifying such exciton condensates, as well as novel applications for memory and logic, even if perhaps limited to growing realm of cryogenic computing in practice if not simulation. We also note that, although not specifically addressed here, again in the experimental III-V [3,21] and simulated graphene-based [14] systems considered previously, one can move smoothly between these two regimes of intralayer and interlayer bias, subject to a conserved net total critical current between the two layers, which offers additional experimental and device possibilities, perhaps particularly so given the ability to combine critical current conservation as seem previously [10,21], with the ability to gate off current flow as a whole by removing electron-to-hole band overlap in such a gapped system.

Finally, we note that we only used a simplified two-band model for the TMD monolayers in this study, which ignores, e.g., the spin-orbit-coupling near the band edges. However, it captures many key band features including the parabolic band structure near the band edges and the existence of the band gaps, which were not considered in an earlier study [14]. Also this method can be easily generalized to more complex and realistic material models, subject only to computational resources.

ACKNOWLEDGMENTS

This work was supported by the Nanoelectronics Research Initiative (NRI) of the Semiconductor Research Corporation (SRC) via the South West Academy of Nanoelectronics (SWAN). Supercomputing resources were provided by the Texas Advanced Computing Center (TACC).

[1] J. P. Eisenstein and A. H. MacDonald, Nature (London) **432**, 691 (2004).
[2] E. Tutuc, M. Shayegan, and D. A. Huse, Phys. Rev. Lett. **93**, 036802 (2004).
[3] D. Nandi, A. D. K. Finck, J. P. Eisenstein, L. N. Pfeiffer, and K. W. West, Nature (London) **488**, 481 (2012).
[4] X. Liu, K. Watanabe, T. Taniguchi, B. I. Halperin, and P. Kim, Nat. Phys. **13**, 746 (2017).
[5] H. Min, R. Bistritzer, J.-J. Su, and A. H. MacDonald, Phys. Rev. B **78**, 121401 (2008).
[6] A. Perali, D. Neilson, and A. R. Hamilton, Phys. Rev. Lett. **110**, 146803 (2013).
[7] G. W. Burg, N. Prasad, K. Kim, T. Taniguchi, K. Watanabe, A. H. MacDonald, L. F. Register, and E. Tutuc, Phy. Rev. Lett. **120**, 177702 (2018).
[8] S. K. Banerjee, L. F. Register, E. Tutuc, D. Reddy, and A. H. MacDonald, IEEE Electron Device Lett. **30**, 158 (2009).
[9] D. Reddy, L. F. Register, E. Tutuc, and S. K. Banerjee, IEEE Trans. Electron Devices **57**, 755 (2010).
[10] X. Mou, L. F. Register, A. H. MacDonald, and S. K. Banerjee, IEEE Trans. Electron Devices **64**, 4759 (2017).
[11] F.-C. Wu, F. Xue, and A. H. MacDonald, Phys. Rev. B **92**, 165121 (2015).
[12] O. L. Berman and R. Y. Kezerashvili, Phys. Rev. B **93**, 245410 (2016).
[13] B. Debnath, Y. Barlas, D. Wickramaratne, M. R. Neupane, and R. K. Lake, Phys. Rev. B **96**, 174504 (2017).
[14] X. Mou, L. F. Register, A. H. MacDonald, and S. K. Banerjee, Phys. Rev. B **92**, 235413 (2015).
[15] X. Wu, X. Mou, L. F. Register, and S. K. Banerjee, in *2015 International Conference on Simulation of Semiconductor Processes and Devices (SISPAD)* (IEEE, Washington, DC, USA, 2015), p. 124.
[16] X. Wu, X. Mou, L. F. Register, and S. K. Banerjee, in *2016 International Conference on Simulation of Semiconductor Processes and Devices (SISPAD)* (IEEE, Nuremberg, Germany, 2016), p. 89.
[17] N. Marzari, A. A. Mostofi, J. R. Yates, I. Souza, and D. Vanderbilt, Rev. Mod. Phys. **84**, 1419 (2012).
[18] B. Fallahazad, K. Lee, S. Kang, J. Xue, S. Larentis, C. Corbet, K. Kim, H. C. P. Movva, T. Taniguchi, K. Watanabe, L. F. Register, S. K. Banerjee, and E. Tutuc, Nano Lett. **15**, 428 (2014).
[19] K. Kim, M. Yankowitz, B. Fallahazad, S. Kang, H. C. P. Movva, S. Huang, S. Larentis, C. M. Corbet, T. Taniguchi, K. Watanabe, S. K. Banerjee, B. J. LeRoy, and E. Tutuc, Nano Lett. **16**, 1989 (2016).
[20] L. F. Register, X. Mou, D. Reddy, W. Jung, I. Sodemann, D. Pesin, A. Hassibi, A. H. MacDonald, and S. K. Banerjee, ECS Trans. **45**, 3 (2012).
[21] D. Nandi, T. Khaire, A. D. K. Finck, J. P. Eisenstein, L. N. Pfeiffer, and K. W. West, Phys. Rev. B **88**, 165308 (2013).
[22] A. Valsaraj, L. F. Register, E. Tutuc, and S. K. Banerjee, J. Appl. Phy. **120**, 134310 (2016).
[23] S. Luryi, Appl. Phys. Lett. **52**, 501 (1988).
[24] M. Li, D. Esseni, G. Snider, D. Jena, and H. G. Xing, J. Appl. Phys. **115**, 074508 (2014).